



Experimental stress analysis of a notched finite composite tensile plate



Abdullah Alshaya*, Robert Rowlands

Dept of Mechanical Engineering, University of Wisconsin-Madison, Madison 53706, WI, USA

ARTICLE INFO

Article history:

Received 14 September 2016

Accepted 8 March 2017

Available online 11 March 2017

Keywords:

Structural composites

Anisotropy

Stress concentration

Digital image correlation

ABSTRACT

Individual displacements and stresses in a vertically-loaded notched finite graphite/epoxy laminated composite are determined by processing measured values of a single component of displacement with an Airy stress function in complex variables. Displacements are recorded using digital image correlation. Traction-free conditions are imposed analytically at the notch using conformal mappings and analytic continuation, and discretely on the vertical free edge. Zero shear stress is also imposed on horizontal line of symmetry. Consequences of employing different amounts and source locations of measured displacements and varying number of coefficients, as well as how displacements are differentiated to provide strains, are considered. Reliability of experimental results is demonstrated by Finite Element and force equilibrium.

© 2017 Elsevier Ltd. All rights reserved.

1. Introduction

Machine and structural members frequently contain holes or notches that produce stress concentrations and can consequently control component integrity. Although composite materials enjoy favorable specific strength and stiffness, their orthotropy influences the stress distributions. Purely analytical or theoretical stress analyses tend to be available for only simple situations involving infinite geometries, whereas many practical problems involve complicated, finite shapes. Moreover, and like numerical approaches such as the finite element method (FEM), analytical/theoretical analyses depend on reliable knowledge of the loading conditions. The latter are commonly unknown in practice. Classical experimental stress analysis approaches suffer from poor results at the edges of cutouts, frequently locations of high mechanical interest. Recognizing these situations, it is advantageous to stress analyze composite structures experimentally by processing DIC-recorded displacement information with a stress function and evaluate reliable edge stresses utilizing analytic continuation.

For plane problems, strain, hence stress, determination from displacements typically necessitates knowing both in-plane components of displacements. However, individual components of

displacement, strain, and stress are available here full-field by processing measured information of a single displacement component using a series representation of an Airy stress function in complex variables. Needing only a single displacement field is advantageous. For example, experimental techniques such as moiré, holography, grids or electronic speckle pattern interferometry (ESPI) necessitate additional rulings and/or optics to record two versus one in-plane component of displacement. Situations can also occur where there is a paucity or inferior quality of one or other of the measured in-plane displacements. Furthermore, such displacement-based techniques necessitate differentiating the recorded data, something which can be unreliable, especially on the edge of the geometric discontinuity (often location of greatest interest) and may lead to highly inaccurate strains and stresses. This latter challenge is overcome here in that the stresses, strains, and displacements at, and in the neighborhood of the notch are obtained from measured information away from the edge of the notch. An additional strength of the present approach is the rigorous mechanics foundation by which strains are determined from measured displacement data.

Khaja, Samad and Rowlands [1,2] obtained the individual stresses in circularly- and elliptically-perforated isotropic plates by processing the recorded displacements with an Airy stress function in real variables using polar coordinates. Recognizing the general inability to analyze orthotropic materials using real variables, several stress analyses of orthotropic composites have utilized an Airy stress function in complex variables and conformal mapping.

* Corresponding author.

E-mail addresses: alshaya@wisc.edu (A. Alshaya), rowlands@engr.wisc.edu (R. Rowlands).

Lin and Rowlands [3] analyzed a notched orthotropic laminated plate thermoelastically, Hawong et al. [4], combined measured isochromatic information and a complex stress function to study the stresses in a circularly-perforated composite whereas Rhee and Rowlands [5] thermoelastically determined the stresses at edge of a circular hole and the stress intensity factors in a composite with a crack. Baek and Rowlands used conformal mapping with moiré [6] and strain gage data [7] to determine the full-field stress around a circular hole in composite plate. Ju and Rowlands [8,9] determined stress intensity factors thermoelastically for inclined cracks in an orthotropic composite while Alshaya et al. [10] employed recorded temperature data to stress analyzed a finite orthotropic composite containing an elliptical hole. All of the prior applications of the mapping technique either separated stresses from isopachic or isochromatic input information or evaluated the stresses using two components of displacement whereas the present approach only used one recorded displacement component to evaluate all the stresses. Ashrafi and Tuttle [11] applied traditional DIC to circularly perforated orthotropic composites but experienced difficulties obtaining reliable results as one approached the edge of the hole.

A finite graphite/epoxy laminated composite plate containing symmetrically-located sided-notches and vertically loaded in the strongest/stiffest material direction is analyzed, Fig. 1. The DIC-recorded displacement data employed are those in the loading direction. This hybrid method does not necessitate knowing the applied loads, smooths the measured displacement data and determines individual stresses throughout, including on the edge of the notch. Experimental reliability is demonstrated by FEM and force equilibrium. The authors are unaware of prior utilization of mapping and complex variables to experimentally evaluate the

stresses in notched composites from displacement data, let alone using only a single measured displacement component.

2. Material and geometry

The finite-width tensile [0₁₃/90₅/0₁₃] graphite/epoxy orthotropic plate (from Kinetic Composites, Inc., Oceanside, CA; $E_{11} = 104 \text{ GPa} = 15.1 \times 10^6 \text{ psi}$, $E_{22} = 28.0 \text{ GPa} = 4.1 \times 10^6 \text{ psi}$, $G_{12} = 2.98 \text{ GPa} = 0.43 \times 10^6 \text{ psi}$, $\nu_{12} = 0.16$) with side notches of radius $R = 12.7 \text{ mm}$ (0.5") was loaded in the strongest/stiffest material direction (1-, y-direction), Fig. 1. Over-all laminate dimensions are 279.4 mm (11") long, 76.2 mm (3") wide and 5.28 mm (0.21") thick. The side notches were machined with a water jet. The coordinate origin is at the center of the plate and the response is symmetric about x- and y-axes. The laminate elastic properties were obtained from conducting uniaxial tensile tests in the strong/stiff (y-direction), weak/compliant (x-direction) and 45-degree orientations [12].

3. Relevant equations

3.1. Complex variable formulation

For plane problems having rectilinear orthotropy and no body forces, the Airy stress function, \mathcal{F} , can be expressed as a summation of two arbitrary analytical functions, $F_1(z_1)$ and $F_2(z_2)$, of the complex variables, z_1 and z_2 , as [13].

$$\mathcal{F} = 2\text{Re}[F_1(z_1) + F_2(z_2)] \quad (1)$$

such that $z_j = x + \mu_j y$ for $j = 1, 2$ and Re denotes the 'real part' of a complex number. The complex material properties μ_1 and μ_2 are two distinct roots of the following equation

$$\mu^4 + \left(\frac{E_{11}}{G_{12}} - 2\nu_{12}\right)\mu^2 + \frac{E_{11}}{E_{22}} = 0 \quad (2)$$

where E_{11} and E_{22} are the elastic moduli parallel and perpendicular to the strongest/stiffest orthotropic direction, G_{12} is the shear modulus, and ν_{12} is Poisson's ratio. The roots of this characteristic equation are complex with $\mu_1 = \alpha + i\beta$, $\mu_2 = \gamma + i\delta$, $\mu_3 = \bar{\mu}_1$, and $\mu_4 = \bar{\mu}_2$. Quantities α , β , γ , and δ are real numbers and both β and δ are positive. The stresses in rectangular coordinates (x, y) of the physical $z (= x + iy)$ plane can be expressed in terms of the stress functions. By introducing the new stress functions

$$\Phi(z_1) = \frac{dF_1(z_1)}{dz_1}, \text{ and } \Psi(z_2) = \frac{dF_2(z_2)}{dz_2} \quad (3)$$

one can write the stresses as

$$\sigma_{xx} = 2\text{Re}[\mu_1^2 \Phi'(z_1) + \mu_2^2 \Psi'(z_2)] \quad (4)$$

$$\sigma_{yy} = 2\text{Re}[\Phi'(z_1) + \Psi'(z_2)] \quad (5)$$

$$\sigma_{xy} = -2\text{Re}[\mu_1 \Phi'(z_1) + \mu_2 \Psi'(z_2)] \quad (6)$$

where primes denote differentiation with respect to the argument. The stresses satisfy equilibrium and associated strains satisfy compatibility. The [0₁₃/90₅/0₁₃] laminate is a balanced, symmetric construction [14]. Hence, in addition to strains being uniform through the thickness, and while 26 plies have their fibers in the loading direction and five plies have their fibers transverse to the

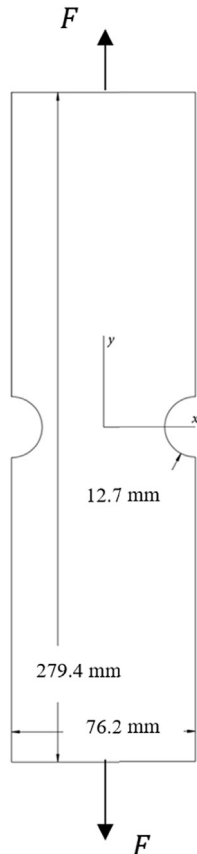


Fig. 1. Vertically-loaded finite Gr/E [0₁₃/90₅/0₁₃] composite plate with circular side notches.

direction of loading, the elastic properties are based on average stresses through the thickness. The stresses of equation (4) through (6) are similarly through-the-thickness average values, i.e., plane stress. The actual stresses in the 90-degree layers are different from those in the 0-degree layers, and both are different from the averaged stresses. The displacements can be written in terms of the stress functions as

$$u = 2\text{Re}[p_1\Phi(z_1) + p_2\Psi(z_2)] - w_0y + u_0 \quad (7)$$

$$v = 2\text{Re}[q_1\Phi(z_1) + q_2\Psi(z_2)] + w_0y + v_0 \quad (8)$$

where w_0 , u_0 , and v_0 are constants of integration and characterize any rigid body translations (u_0 and v_0) and rotation (w_0). The other quantities, which depend on material properties, are

$$p_1 = \frac{\mu_1^2}{E_{11}} - \frac{\nu_{12}}{E_{11}}, \quad p_2 = \frac{\mu_2^2}{E_{11}} - \frac{\nu_{12}}{E_{11}} \quad (9)$$

$$q_1 = -\frac{\nu_{12}}{E_{11}}\mu_1 + \frac{1}{E_{22}\mu_1}, \quad q_2 = -\frac{\nu_{12}}{E_{11}}\mu_2 + \frac{1}{E_{22}\mu_2} \quad (10)$$

When the plate is loaded physically in a testing machine, the rigid body motions, u_0 , v_0 , and w_0 are zero. Plane problems of elasticity classically involve determining the stress functions, $\Phi(z_1)$ and $\Psi(z_2)$, throughout a component and subject to the boundary conditions around its entire edge. For a region of a component adjacent to a traction free-edge, $\Phi(z_1)$ and $\Psi(z_2)$ can be related to each other by the conformal mapping and analytic continuation techniques. The stresses can then be expressed in terms of the single stress function, $\Phi(z_1)$. Moreover, $\Phi(z_1)$ will be represented by a truncated power-series expansion whose unknown complex coefficients are determined experimentally. Once $\Phi(z_1)$ and $\Psi(z_2)$ are fully evaluated, the individual stresses and displacements are known from equation (4) through (8). For a significantly large region of interest in a finite structure, it may also be necessary to satisfy other boundary conditions at discrete locations.

3.2. Conformal mapping

Conformal mapping is introduced to simplify the plane problem by mapping the region R_z of a complicated physical $z = x + iy$ plane of a loaded component into a region R_ζ of a simpler shape in the $\zeta = \xi + i\eta$ plane, the latter being a unit circle if one represents the stress function as a Laurent series, Fig. 2 [13–21]. The new coordinate system (and resulting geometry) is usually chosen to aid in solving the equations and the obtained solution from this simplified domain can then be mapped back to the original physical geometry for a valid solution.

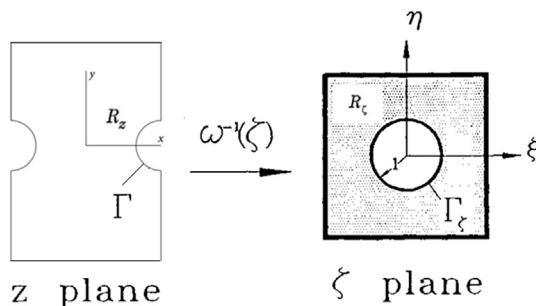


Fig. 2. Mapping circular cutout in the physical z -plane into exterior region of a unit circle in ζ -plane.

Assume that a mapping function of the form

$$z = \omega(\zeta) \quad (11)$$

exists and which maps R_ζ of the simpler plane into R_z of the more complicated physical plane. For orthotropy, auxiliary planes and their induced mapping functions are defined in terms of $\zeta_j = \xi + \mu_j\eta$ so by substituting $z_j = x + \mu_jy$ into equation (11), i.e.,

$$z_j = \omega_j(\zeta_j), \quad j = 1, 2 \quad (12)$$

The induced conformal mapping functions are one-to-one and invertible. The stress functions $\Phi(z_1)$ and $\Psi(z_2)$ can be expressed as the following analytic functions of ζ_1 and ζ_2 ,

$$\Phi(z_1) = \Phi[\omega_1(\zeta_1)] \equiv \Phi(\zeta_1), \quad \Psi(z_2) = \Psi[\omega_2(\zeta_2)] \equiv \Psi(\zeta_2) \quad (13)$$

Derivatives of the stress functions with respect to their argument are

$$\Phi'(z_1) = \Phi'(\zeta_1) \frac{d\zeta_1}{dz_1} = \frac{\Phi'(\zeta_1)}{\omega_1'(\zeta_1)}, \quad \Psi'(z_2) = \frac{\Psi'(\zeta_2)}{\omega_2'(\zeta_2)} \quad (14)$$

The analyticity of the mapping functions satisfies the equilibrium and compatibility throughout region R_z of the physical plane.

3.3. Traction-free boundaries

Using the concept of analytic continuation, the individual stress functions for a region R_ζ adjacent to a traction-free boundary of the unit circle of an orthotropic material are related by Refs. [22,23].

$$\Psi(\zeta_2) = \overline{B\Phi\left(1/\overline{\zeta_2}\right)} + C\Phi(\zeta_2) \quad (15)$$

where B and C

$$B = \frac{\bar{\mu}_2 - \bar{\mu}_1}{\mu_2 - \bar{\mu}_2}, \quad C = \frac{\bar{\mu}_2 - \mu_1}{\mu_2 - \bar{\mu}_2} \quad (16)$$

Equation (15) enable the elastic strains and stresses of the structure to be expressed in terms of a single stress function, $\Phi(\zeta_1)$, the latter which can be represented by a Laurent series expansion. Equation (15) assumes ability to map the physical boundary of interest into either the unit circle or the real axis in the mapped plane. Reference [24] contains a simple, clear derivation of equation (15).

3.4. Mapping formulation

For a region adjacent the circular notch of radius R , the following function [17].

$$z_j = \omega_j(\zeta_j) = \frac{R}{2} \left[\left(1 - i\mu_j\right)\zeta_j + \frac{1 + i\mu_j}{\zeta_j} \right], \quad j = 1, 2 \quad (17)$$

maps the region of the exterior of a unit circle, R_ζ , of the ζ -plane into the region R_z of the z -physical plane, Fig. 2. The derivative of this mapping function is

$$\omega_j'(\zeta_j) = \frac{R}{2} \left[\left(1 - i\mu_j\right) - \frac{1 + i\mu_j}{\zeta_j^2} \right], \quad j = 1, 2 \quad (18)$$

and the inverse of the induced mapping function is

$$\zeta_j = \omega_j^{-1}(z_j) = \frac{z_j \pm \sqrt{z_j^2 - R^2(1 + \mu_j^2)}}{R(1 - i\mu_j)}, j = 1, 2 \quad (19)$$

The branch of the square root in equation (19) is chosen such that $|\zeta_j| \geq 1$ for $j = 1, 2$.

3.5. Mapping collocation, stresses and displacements

The single stress function can be expressed as the following finite Laurent series [17].

$$\Phi(\zeta_1) = \sum_{\substack{j=-N \\ j \neq 0}}^N A_j \zeta_1^j \quad (20)$$

where $A_j = a_j + ib_j$ are the unknown complex coefficients (a_j and b_j are both real numbers). The $j = 0$ term contributes to rigid-body motion and can be omitted. Substituting equation (20) into (15) yields

$$\Psi(\zeta_2) = \sum_{\substack{j=-N \\ j \neq 0}}^N (\bar{A}_j B \zeta_2^{-j} + A_j C \zeta_2^j) \quad (21)$$

where \bar{A}_j is the complex conjugate of A_j . At least for a finite, simply connected region R_ζ , $\Phi(\zeta_1)$ is a single-valued analytic function. Orthotropic composite whose complex parameters are purely imaginary when the directions of material symmetry are parallel and perpendicular to the applied load require that only odd terms be retained in the Laurent expansions. Upon combining equation (4) through (6), (14), (20), and (21) the individual stresses become

$$\sigma_{xx} = 2 \sum_{\substack{j=-N, -N+2, \dots \\ j \neq 0}}^N \operatorname{Re} \left\{ j \left[\frac{\mu_1^2 \zeta_1^{j-1}}{\omega_1'(\zeta_1)} + \frac{C \mu_2^2 \zeta_2^{j-1}}{\omega_2'(\zeta_2)} \right] A_j - j \mu_2^2 B \left[\frac{\zeta_2^{j-1}}{\omega_2'(\zeta_2)} \right] \bar{A}_j \right\} \quad (22)$$

$$\sigma_{yy} = 2 \sum_{\substack{j=-N, -N+2, \dots \\ j \neq 0}}^N \operatorname{Re} \left\{ j \left[\frac{\zeta_1^{j-1}}{\omega_1'(\zeta_1)} + \frac{C \zeta_2^{j-1}}{\omega_2'(\zeta_2)} \right] A_j - j B \left[\frac{\zeta_2^{j-1}}{\omega_2'(\zeta_2)} \right] \bar{A}_j \right\} \quad (23)$$

$$\sigma_{xy} = -2 \sum_{\substack{j=-N, -N+2, \dots \\ j \neq 0}}^N \operatorname{Re} \left\{ j \left[\frac{\mu_1 \zeta_1^{j-1}}{\omega_1'(\zeta_1)} + \frac{C \mu_2 \zeta_2^{j-1}}{\omega_2'(\zeta_2)} \right] A_j - j \mu_2 B \left[\frac{\zeta_2^{j-1}}{\omega_2'(\zeta_2)} \right] \bar{A}_j \right\} \quad (24)$$

From equations (7) and (8), the displacements can be written as

$$u = 2 \sum_{\substack{j=-N, -N+2, \dots \\ j \neq 0}}^N \operatorname{Re} \left\{ [p_1 \zeta_1^j + p_2 C \zeta_2^j] A_j + p_2 B \zeta_2^{-j} \bar{A}_j \right\} \quad (25)$$

$$v = 2 \sum_{\substack{j=-N, -N+2 \\ j \neq 0}}^N \operatorname{Re} \left\{ [q_1 \zeta_1^j + q_2 C \zeta_2^j] A_j + q_2 B \zeta_2^{-j} \bar{A}_j \right\} \quad (26)$$

The only unknowns in these expressions for the stresses and displacements are the complex coefficients $A_j = a_j + ib_j$, the other quantities involve geometry (location) or material properties. Because the summation in equation (22) through (26) involves only the odd values of N , the number of complex coefficients, A_j , is $N + 1$ and the number of real coefficients, a_j and b_j , is $2(N + 1)$. These coefficients can be determined from measured displacement data. It should be noted that by using conformal mapping and analytic continuation techniques, equation (22) through (24) imply that the stresses satisfy equilibrium and traction-free conditions in the adjacent portion of the entire boundary. However, unlike a classical boundary-value problem where one would typically evaluate the unknown coefficients, A_j , by satisfying the boundary and loading conditions around the entire shape, one can use a combination of the measured stresses of equation (22) through (24) and/or displacements of equations (25) and (26) from within region R_z to determine these unknown complex coefficients, A_j . Additional known boundary conditions may also be imposed at discrete locations. The concept of collecting measured data in a region R^* adjacent to an edge Γ , mapping R_z into R_ζ such that Γ of the physical z -plane is mapped into the unit circle in the ζ -plane whereby the traction-free conditions on Γ are satisfied continuously, relating the two complex stress functions to each other, plus satisfying other loading conditions discretely on the boundary of the component beyond Γ will be referred to as the mapping-collocation technique.

The interior displacement data v^* at m different locations within region R^* and q known stress conditions (in terms of σ_{xy}) at discrete points along the free outer surface and line of symmetry ($y = 0$) are employed, Fig. 1. A system of simultaneous linear equations $[V]_{(m+q) \times 2(N+1)} \{C\}_{2(N+1) \times 1} = \{V^*\}_{(m+q) \times 1}$, is formed whose matrix $[V]$ consists of analytical expressions of displacement component v^* , equation (26), and the expressions of the known stress conditions, vector $\{C\} = \{a_{-N}, b_{-N}, a_{-N+2}, b_{-N+2}, \dots, a_{N-2}, b_{N-2}, a_N, b_N\}$ has $2(N + 1)$ unknown real coefficients, and vector $\{V^*\}$ includes the m measured displacement values of v^* and q discretely imposed stress conditions such that $m + q \gg N + 1$. The best values of the coefficients A_j , in a least-squares numerical sense, can then be determined. The variables $\zeta_j = \xi + \mu_j \eta$, in equation (22) through (26) are related to the physical locations $z = x + iy$ through the inverse mapping function $z_j = \omega_j(\zeta_j)$ of equation (17) through (19). The individual stresses then are known throughout the region R_z , including on the traction-free edge Γ from equation (22) through (24). As will be discussed subsequently, the number of terms, N , to retain in the stress function was selected by evaluating the difference between the magnitude of experimentally based displacement data and those predicted according to the present hybrid method by using root mean square approach.

4. Digital image correlation

Digital Image Correlation (DIC) is a full-field computer-based image analysis technique for the non-contact measurement of displacements of a surface equipped with a speckle pattern. The method tracks the motion of the speckles by comparing the grey scale value at a point (subset) in a deformed and undeformed configuration. Two sets of images are recorded; the first image typically being at zero load and the second image under load. A single camera setup can record both u and v in-plane full-field deformations. Out-of-plane motions can also be recorded if two

cameras are employed. The achievable DIC resolution depends on a number of factors, including but not limited to, camera resolution, lens optical quality, and speckle size and quality. Unlike electronic speckle, DIC necessitates the surface under study to have a speckle pattern for tracking; but unlike thermoelectric stress analysis, DIC does not require cyclic loading. Table 1 contains the DIC analysis details.

Vic-Snap software (by Correlated Solutions, Inc., Columbia, SC, USA, [25]) was used to record the images of the plate in its loaded and unloaded conditions and to evaluate the displacements for post-processing. When utilizing two cameras, a separate calibration grid (provided by Correlated Solution with the DIC package) was used to evaluate the displacement data in physical units rather than in pixels. Rather than using the Vic-Snap software to provided strains, the DIC-recorded v -displacement (vertical) data were processed using the Airy stress function. Quality displacement information at and near the edge of the notch and at (near) the longitudinal edge of the specimen is unavailable because the DIC software's correlation algorithm is unable to track a group of pixels (subset) which lack neighboring pixels. To perform the tracking, the subset is shifted until the pattern in the deformed image closely matches that of the reference image.

The measured DIC data were digitalized in matrix form and combined with the Airy stress function to determine the stresses. Recognizing one has fewer complex coefficients to evaluate than amount of data from which to evaluate them, the coefficients were determined using least squares. Although the recorded displacement data at, and adjacent to, an edge are unreliable and raw displacement information in composites is inherently noisy, the present technique overcomes these challenges by avoiding the use of recorded data on and near edges and by processing the measured interior data with a stress function, mapping and analytic continuation. The resulting reliable DIC-determined stresses are available on and in the neighborhood of the edge of the hole without knowing the distant geometry, loading or boundary conditions.

4.1. Plate preparation and loading

A random speckle pattern of white dots on a black background was applied to the composite's surface. The plate was statically loaded in the hydraulic grips of a 20 kips capacity MTS hydraulic testing machine from 0 N to 7117 N (1600 lb) in 890 N (200 lb) load increments, Fig. 3. Displacement data were recorded and processed at each load increment. Before conducting the quantitative analysis, two cameras were used to capture the three displacement components by which to verify there was no out-of-plane bending [21].

Table 1

Technical information about the DIC equipment, set-up, and system.

Parameter	Setting
Technique	Stereo Image Correlation
Cameras	The Grasshopper (Point Grey Research), Model GRAS-5055M-C
Imaging sensor	Sony ICX625 CCD, 2/3", 3.45 μm
Lens	CM120 BK 15 COMPACT-0901 (focal ratio: 1.9 and focal length: 35 mm)
Sensor/digitization	2448 \times 2048 at 15 FPS
Lightening	Ambient white light
Pixel to inch conversion	1 pixel = 0.025 mm (0.01 inch)
Software	Vic-Snap software by Correlated Solutions, Inc.
Subset, step	17, 5
Strain Resolution	0.005% (50 microstrain)

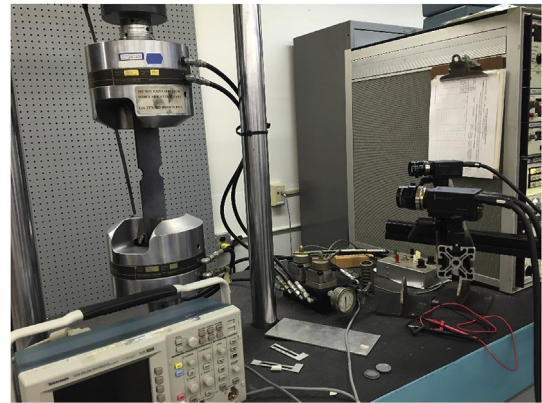


Fig. 3. Experimental setup.

4.2. DIC recording

The recorded v -displacement information, Fig. 4a, was exported to MATLAB (Mathworks, Inc., 2015) to convert each pixel into a data point, i.e., points like those in Fig. 5b. Since DIC data typically are unreliable on and near an edge, no recorded displacements were used within at least 2.95 mm = 0.12 inch of the boundary of the notch. The u -displacement are relatively small and their DIC-evaluated values are not as reliable as the v -displacements. Although not appreciated a priori, this turned out to be an example where one of the two displacement fields is not highly reliable but by using the present hybrid technique, one could obtain displacement information in one direction from that in the other direction. One can moreover evaluate the full-field individual stresses and strains without physically differentiating the displacements.

4.3. Data processing

The individual stresses were determined throughout the region containing the notch from the raw v -displacement data of Fig. 4 using the mapping-collocation technique. The DIC correlated solution software provided approximately 102,200 values of v when the analysis was carried out for 17 subsets in 5 steps. The plate is geometrically and mechanically symmetrical about the vertical y -axis. Since the top end of the physically tested plate was fixed stationary while the bottom end moved vertically downward, Fig. 3, the zero vertical displacement was shifted to be at the horizontal middle of the plate, Fig. 4b, to represent the case of the plate being extended at both top and bottom ends. The measured v -displacement data of Fig. 4b were subsequently averaged about all quadrants to cancel any asymmetry and the resulting averaged measured values of 17,666 v -displacement data are plotted in the second quadrant as shown in Fig. 5a. For the subsequently used mathematical mapping, the coordinate origin was also transferred to the center of the left notch. Due to the previously mentioned unreliability, recorded data on and near the edge of the notch were not employed. Only 2200 of the available 17,666 v -displacements were selected randomly and used. Their source locations are shown in Fig. 5b. The region of Fig. 5b is denoted as region R^* . Like most experimental data, the measured data incorporate some noise which necessitate collecting more measured input values than the number of unknown coefficients of a stress function. In addition to the selected v -displacements associated with Fig. 5b, $\sigma_{xy} = 0$ of equation (24) was imposed at each of 12 equally-spaced discrete locations along the left vertical traction-free edge of the plate and along the horizontal line of symmetry, $y = 0$. The total number of equations (side conditions), $m + q$, where $m = 2200$ and $q = 24$,

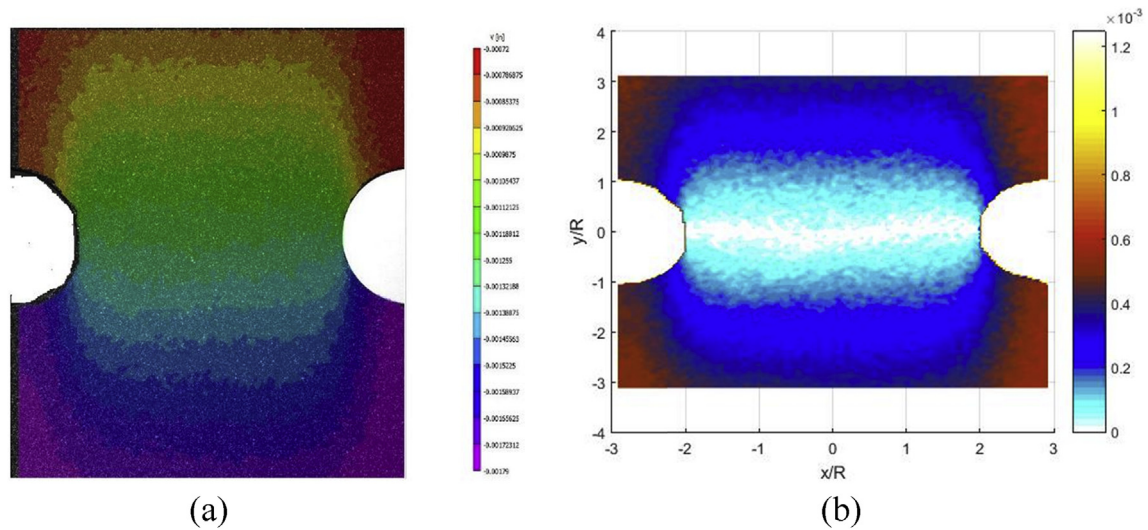


Fig. 4. DIC recorded ν -displacement data (a) from Vic-snap software and (b) after shifting the zero displacement ν to vertical middle of plate (loaded at 7117 N = 1600 lb).

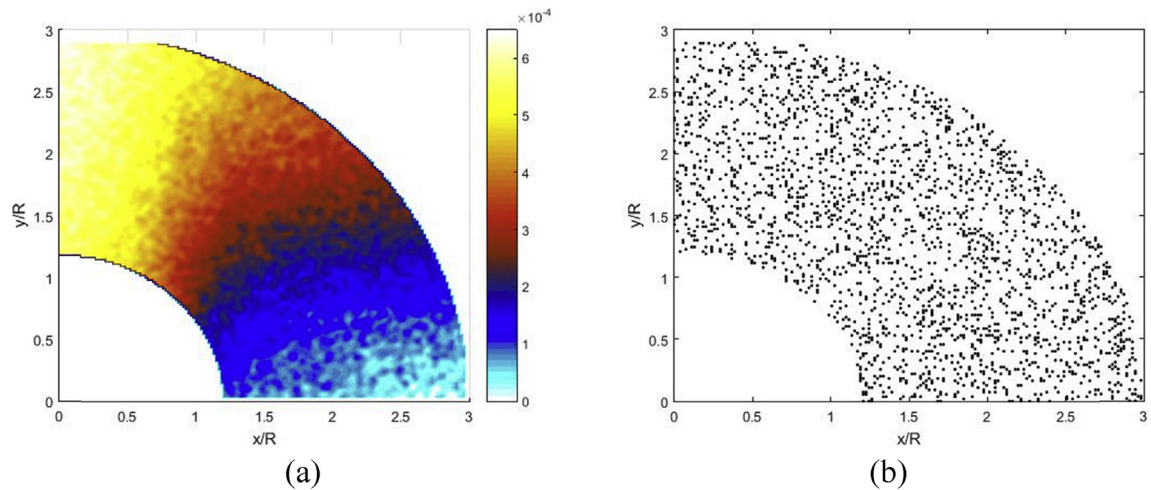


Fig. 5. (a) Averaged recorded ν -displacement data from Vic-snap from all four quadrants; (b) source locations of $m = 2200$ DIC values.

exceeds the number of real coefficients, $2(N + 1)$, producing an overdetermined system which can be solved using a least-squares. The system was solved in MATLAB using the backslash ‘\’ operator.

4.4. Evaluating number of coefficients to employ

The coefficients, $A_j = a_j + ib_j$, were evaluated using equation (17) through (19) to map the physical plane into the unit circle in the ζ -plane. The unreliable ν -displacement values on and near the boundary of the side notch motivated using only ν -displacements originating at locations shown in Fig. 5b. The magnitude of the complex coefficients, A_j , were determined from equation (26) using the measured ν -displacement data located inside the region R^* , Fig. 5b, and imposing zero shear stress discretely along the outer left vertical free surface and the line of symmetry, $y = 0$. The individual stresses were evaluated throughout region R_z using equation (22) through (24) including along edge Γ , Fig. 2, where no ν -displacement input data were employed.

One must assess how many coefficients to employ in the stress function. Using too few coefficients gives inaccurate results, while too many can make the matrix, $[V]$, unstable or even singular due to

computer round-off and quantization errors. The number of real coefficients, $2(N + 1)$, to retain was selected by comparing, using the root mean square approach, the difference between the magnitudes of the DIC recorded ν -displacements with those predicted by least-square from equation (26) and the 24 zero shear conditions as a function of the number of evaluated coefficients, Fig. 6. This plot suggests using 6 complex (12 real) coefficients. The suitability of utilizing 12 real coefficients is supported by comparing the recorded ν -displacement data with the reconstructed image based on equations (26) and (12) real coefficients, Fig. 7. Subsequent discussion illustrates the effects on the stress concentration of employing different number of coefficients, whereas reference [21] compares recorded and reconstructed figures of ν -displacement for varying number of coefficients.

5. Finite element analysis

In order to provide some results with which to compare those from DIC, a finite element analysis (FEA) using ANSYS (ANSYS, Inc, Academic Research, Release 16.2. 2015) was prepared of the composite plate of Fig. 1. Due to symmetry, only one quarter of the plate

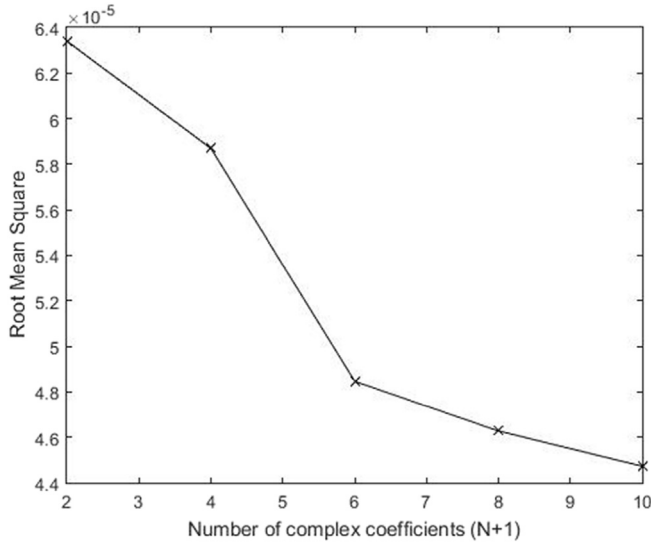


Fig. 6. Root Mean Square value for different number of complex coefficients, $N+1$.

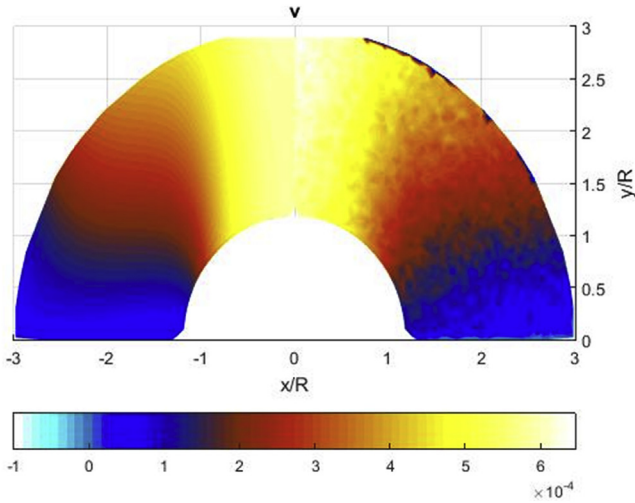


Fig. 7. Comparison of ν -displacement throughout region adjacent to hole from recorded DIC (right) and reconstructed using hybrid-DIC; $m = 2,200$, $q = 24$ and 12 real coefficients (left).

was modeled with symmetrical boundary condition applied at the bottom and right edges. A far-field stress of

$$\sigma_0 = \frac{F}{A} = \frac{7117.2 \text{ N}}{0.52 \text{ cm} \times 7.62 \text{ cm}} = 17.96 \text{ MPa} = 2604 \text{ psi}$$

was applied numerically to the top edge. Eight-node isoparametric plane 82 element were employed. A very fine mesh was used in the neighborhood of the circular notch. A convergence test was applied until the change in magnitude of the maximum stress between two successive meshing was less than 2%. The FE quarter model utilizes 7500 elements and 7701 nodes. Reference [21] contains additional details of the ANSYS analysis and associated results.

6. Results

6.1. Stresses and displacements

The tangential stress, $\sigma_{\theta\theta}$, normalized by the far-field stress,

$\sigma_0 = 17.96 \text{ MPa}$, is plotted on the boundary of the notch in Fig. 8. The hybrid-DIC based results agree with the FEM predictions. The ANSYS and hybrid-DIC determined stress concentrations are 7.37, and 7.48, respectively.

Contour plots of normalized polar components of stress and displacement from hybrid-DIC and ANSYS are compared in Figs. 9 and 10. There is excellent agreement between the ANSYS-predicted values and the hybrid technique using $m = 2200$ ν -displacement values.

6.2. Load equilibrium

To further assess reliability of the present hybrid-DIC method, load equilibrium based on DIC-determined stress was compared with the physically applied load. This was done by numerically integrating the vertical stress σ_{yy} along the line $y = 0$ in Fig. 1.

$$F = \int \sigma_{yy} dA = 2 \int_R^{W/2} \sigma_{yy} t dx \quad (27)$$

where t is the plate thickness. The integration was computed using the trapezoidal rule. The computed load based on hybrid-DIC stress is 7.10 kN (1596 lb), which is 0.25% less than the physically applied load of 7.12 kN (1600 lb).

6.3. Effect of variations in number of coefficients employed

Figs. 6 and 7 suggest using 6 complex (12 real) coefficients. Fig. 8 through 10 indicate these give accurate results. However, results of Table 2 demonstrate reliable DIC-determined values for the stress concentration factor at the notch when employing at least two to 10 complex coefficients.

6.4. Magnitudes of coefficients A_j

Table 3 lists the magnitudes of experimentally-determined coefficients A_j of equation (26) associated with ν -displacement data. The data demonstrate the dominating influence of the early coefficients but the reduced consistency in magnitudes of the coefficients with increasing of N . On the other hand, in addition to the

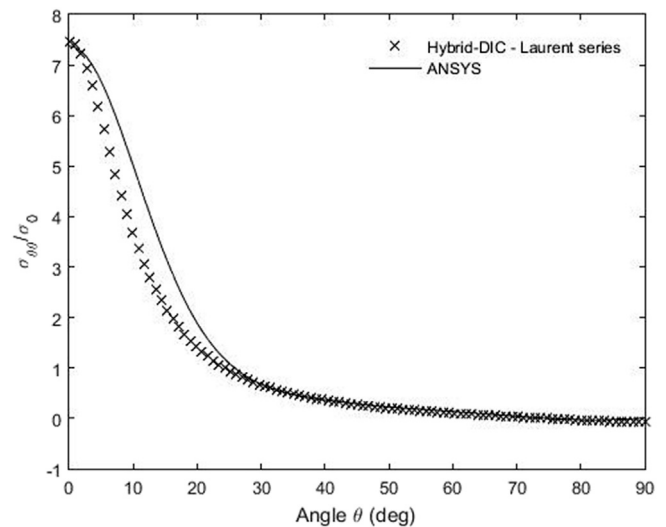


Fig. 8. Variation of $\sigma_{\theta\theta}/\sigma_0$ along boundary of notch from FEA and hybrid-DIC; $m = 2,200$, $q = 24$ and 12 real coefficients.

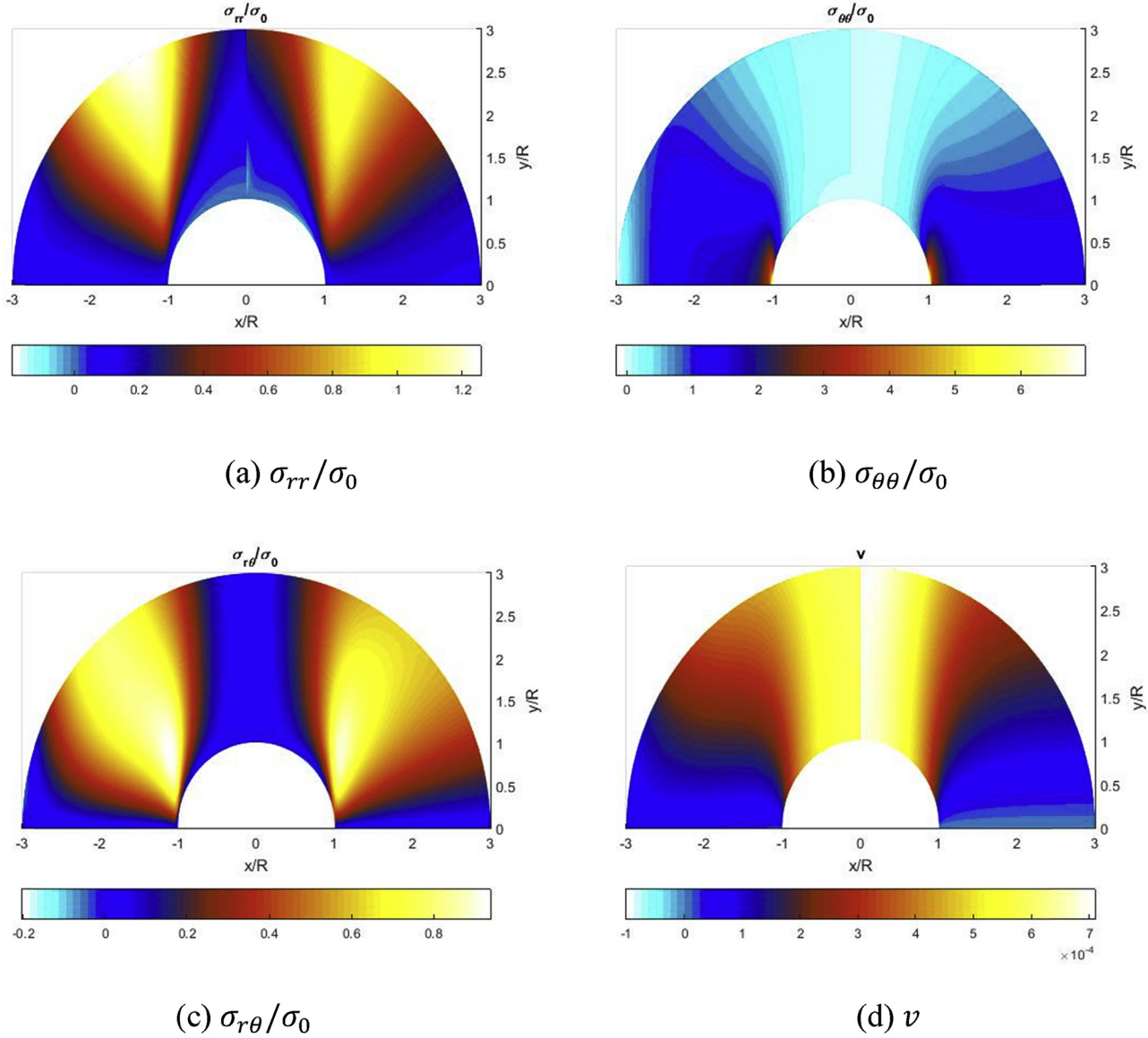


Fig. 9. Contour plot of (a) σ_{rr}/σ_0 ; (b) $\sigma_{\theta\theta}/\sigma_0$; (c) $\sigma_{r\theta}/\sigma_0$; and (d) v throughout the region adjacent to the notch by FEA (right) and hybrid-DIC; $m = 2,200$, $q = 24$ and 12 real coefficients (left).

fact that lower-order a_j coefficients of equation (26) dominate, the values of these a_1 and a_{-1} tend to be very consistent for all values of N considered.

6.5. Amount of and source locations of input data

Results of Figs. 8 and 10 and Table 2 demonstrate that the DIC-determined and ANSYS-predicted stress concentration factors agree. However, these results are based on the 2200 recorded input v -displacements selected randomly from the available 17,666 values of region R^* in Fig. 5a. It is informative to consider how the magnitude of the stress concentration factor and predicted load from equation (27) depend on the amount and source locations of measured input data. A MATLAB subroutine was used to change randomly the amount and source locations of measured input v -displacement data employed in the region between $1.2R$ and $3R$ (retaining the same additional 24 zero shear stress conditions along the left vertical traction-free edge and the horizontal line of symmetry, $y = 0$). This routine was repeated 10 times and the resulting

mean and standard deviation values for the stress concentration factor and calculated applied load are plotted in Figs. 11 and 12, respectively. The figures show that the results converge at approximately 1000 recorded input data of the originally available 17,666 v -displacements. The plot of the calculated applied load is only used to show the reliability of the results for each set of input data. Reference [26] provides helpful information on the amount and source locations of the thermoelastic stress (TSA) input data, and number of coefficients, to employ. However unlike reference [26], the present amount and source locations of the displacement input were generated and selected randomly and not necessarily uniformly. This assesses the effects on the reliability of such DIC techniques of varying the amount and source locations of the recorded input data.

6.6. Comparison with correlated solutions

Recognizing recorded DIC data are unreliable at and close to an edge, there is merit in not employing such information along

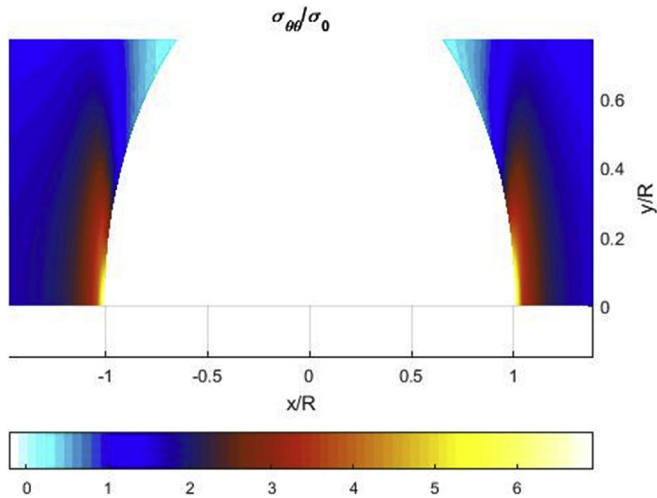


Fig. 10. Enlarged view of $\sigma_{\theta\theta}/\sigma_0$ of Fig. 9(b) in region adjacent to the notch by FEA (right) and hybrid-DIC; $m = 2,200$, $q = 24$ and 12 real coefficients (left).

Table 2

Stress concentration factor (maximum $\sigma_{\theta\theta}/\sigma_0$) at notch in finite-width $[0_{13}/90_5/0_{13}]$ plate for varying number of Airy coefficients ($m = 2200$ and $q = 24$).

ANSYS	N (number of real coefficient)	Hybrid-DIC (percentage difference with ANSYS)
7.37	1 (4)	6.88 (6.6%)
	3 (8)	7.17 (2.7%)
	5 (12)	7.48 (1.5%)
	7 (16)	7.59 (3.0%)
	9 (20)	7.57 (2.7%)

Table 3

Magnitudes of individual coefficients associated with the stress calculation in notched, $[0_{13}/90_5/0_{13}]$ graphite/epoxy plate using DIC data as a function of N ($m = 220$ and $q = 24$).

Coefficients	$N = 1$	$N = 3$	$N = 5$
a_1	-63.54	-63.93	-62.66
b_1	4.32	2.45	2.75
a_{-1}	-64.39	-65.15	-64.50
b_{-1}	-3.06	-1.74	-1.95
a_3		0.67	1.95
b_3		0	0
a_{-3}		0.76	2.25
b_{-3}		0	0
a_5			0.068
b_5			0
a_{-5}			0.075
b_{-5}			0

edges and it can be challenging to obtain reliable stress concentration factors. Strains in the vertical y -direction, ϵ_{yy} , along the line $y = 0$ in Fig. 1 from FEA, hybrid-DIC, and Correlated Solution's commercial Vic snap software are compared in Fig. 13. Unlike Correlated Solution's differentiation method for determining strains, and without changing correlation parameters (subset, step, filter size) as in Ref. [11], the present DIC method determines the strains from measured displacements based on a rigorous mechanics foundation (Airy stress function, equilibrium and compatibility). Reference [2] reported similar discrepancy in strains computed using commercial DIC software and those from FEM and strain gages.

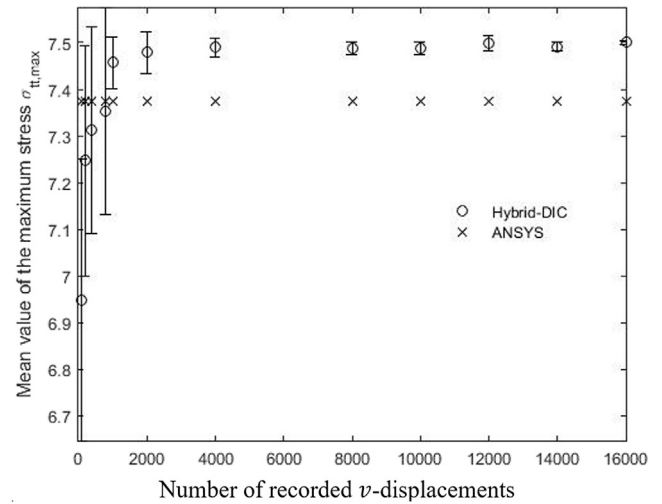


Fig. 11. Mean and standard deviation of DIC-determined stress concentration factor at notch using different varying random source locations and amounts of DIC-recorded values of v (12 real coefficients; $q = 24$).

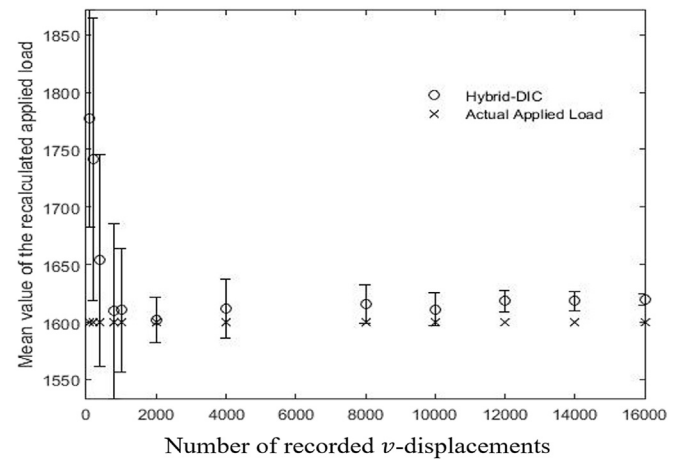


Fig. 12. Mean and standard deviation of DIC-based load using different varying random source locations and amounts of DIC-recorded values of v (12 real coefficients; $q = 24$).

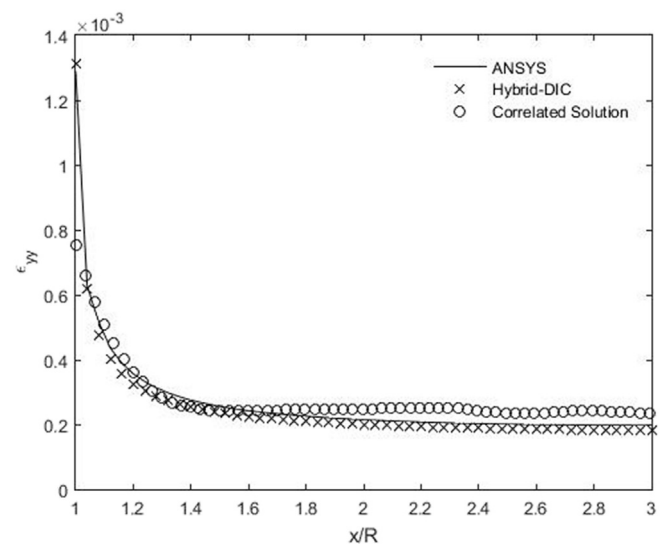


Fig. 13. Strain ϵ_{yy} along line $y = 0$ in Fig. 1 from ANSYS, hybrid-DIC ($m = 2,200$, $q = 24$ and 12 real coefficients) and Correlated Solutions.

7. Summary, discussion and conclusions

Stresses and strains at and in the vicinity of the edge of a side notch in a uniaxially-loaded finite graphite/epoxy composite are determined by processing DIC-recorded values of a single component of displacement with an Airy stress function in complex variables. Reliability of experimental results is demonstrated by Finite Element and force equilibrium. The consequences of employing different random sets of measured input data, varying the number of coefficients and the manner in which displacements are differentiated to provide strains are considered. Most of the present results are based on 12 real coefficients and 2200 measured input displacements, but information shows acceptable values of the stress concentration at the notch root when using between 8 and 20 real coefficients and 1000 or more measured input displacements. The dominating influence of the early coefficients and reduced consistency in magnitudes for subsequent coefficients is noted.

In theory, one can choose to use either recorded u - or v -displacement data. For example, reference [27] evaluates and compares the magnitudes of the Airy coefficients independently from each of the recorded two in-plane displacements. However, barring other considerations, one usually employs the displacement component having the anticipated largest magnitude. Upon evaluating the Airy coefficients from the relevant equation (25) or (26), the stresses are available from equation (22) through (24). No assumption or use is typically made of the other displacement. If wanted, the other displacement values can be determined from the determined Airy coefficients (Table 3) and the appropriate equation (25) or (26).

The authors are unaware of any previously published determination of the individual stresses full-field in a side-notched orthotropic laminate from recorded information of a single displacement field. An objective of the present paper is to be able to stress analyze orthotropic cases experimentally which cannot be analyzed numerically. Having said that, the geometry and loading of Fig. 1 were selected to provide a reliable FEM prediction with which to validate the hybrid-experimental approach. Unlike here, it is not uncommon to have engineering structures whose external loads are unknown, thereby precluding using FEM. For example, ship or airplane members such as bulkheads and wing ribs and spars often contain cutouts and the external loads on such structures can be unknown. In such situations, and unlike presently, the directions of material symmetry might not coincide with the direction of loading. This could be addressed by rotating the xy -coordinates relative to the loading direction to retain the x - and y -axes aligned in the directions of material symmetry. Although the current problem involves four-quadrant symmetry, the method described is not restricted to symmetry. In fact one might employ Schwarz–Christoffel mapping for highly complicated geometries. However, equation (15) presupposes ability to map the physical boundary of interest into either the unit circle or the real axis in the mapped plane. If that is not feasible, rather than employ equation (15), one could represent the stress functions $\Phi(z_1)$ and $\Psi(z_2)$ as independent series [28]. Since the current approach assumes plane stress, cases such as out-of-plane bending or variations in thickness would require other considerations. While DIC-recorded displacement data are utilized here, one could employ moiré, ESPI, or holographic techniques.

Acknowledgement

Abdullah Alshaya was funded by a graduate scholarship from the Kuwait University. The authors thank Jacob Zeuske for his technical assistance. This research did not receive any specific grant

from funding agencies in the public, commercial, or not-for-profit sectors.

Nomenclature

A_j	Complex coefficients $A_j = a_j + ib_j$
\bar{A}_j	Complex conjugate of A_j
B, C	Complex material properties
$\{c\}$	Vector of unknown coefficients
E_{11}, E_{22}	Elastic moduli in material directions
F	Applied load
$F_1(z_1), F_2(z_2)$	Arbitrary analytical functions
\mathcal{F}	Airy stress function
$\mathcal{F}(x, y)$	Airy stress function in rectangular coordinate
G_{12}	Shear moduli
Im	Imaginary part
m	Number of measured input displacements
N	Terminating integer of the summation series
p_1, p_2, q_1, q_2	Complex material properties
q	Number of known stress conditions
r, θ	Polar coordinates
R	Radius of notch
R^*	Region in which data were selected
Re	Real part
R_z	Region in the physical plane (x, y)
R_ζ	Mapped region of R_z in ζ -plane (ξ, η)
RMS	Root Mean Square
t	Thickness of plate
u, v, w	Cartesian displacements in x -, y -, and z -directions
$[V]$	Analytical expression of displacement component v^* and other expression of the known stress conditions
$\{V^*\}$	Matrix of m measured displacement values of v^* and q discrete points with known stress conditions
W	Width of plate
x, y	Cartesian (rectangular) coordinates
z_1, z_2	Complex variable; $z_j = x + \mu_j y$ for $j = 1, 2$
α and γ	Distinct real parts of complex parameters μ_k
β and δ	Distinct imaginary parts of complex parameters μ_k
Γ	Traction-free boundary in physical plane R_z
Γ_ζ	Mapped traction-free boundary, Γ , in ζ -plane R_ζ
ζ, ξ, η	Coordinates in the mapped plane
μ_k	Roots of characteristic equation associated with the compatibility equation
ν_{12}	Poisson's ratio
σ_o	Far-field applied normal stresses
σ_{11}, σ_{22}	Normal stresses in the direction of material symmetry
$\sigma_{rr}, \sigma_{\theta\theta}, \sigma_{r\theta}$	Stresses in polar coordinate (radial, tangential, and shear stresses)
$\sigma_{xx}, \sigma_{yy}, \sigma_{xy}$	Stresses in Cartesian coordinate
Σ	Summation
$\Phi(z_1)$	Stress function $\Phi(z_1) = dF_1(z_1)/dz_1$
$\Psi(z_2)$	Stress function $\Psi(z_2) = dF_2(z_2)/dz_2$
$\omega(\zeta)$	Mapping function
\backslash	Backslash operator (MATLAB)

References

- [1] A.A. Khaja, D.R. Matthys, R.E. Rowlands, Determining all displacements, strains and stresses full-field from measured values of a single displacement component, *Exp. Mech.* 54 (2014) 443–455, <http://dx.doi.org/10.1007/s11340-013-9818-2>.
- [2] W. Samad, R. Rowlands, *Nondestructive Full-field Stress Analysis of a Finite Structure Containing an Elliptical Hole Using Digital Image Correlation*, 2012.
- [3] S.T. Lin, R.E. Rowlands, Thermoelastic stress analysis of orthotropic composites, *Exp. Mech.* 35 (1995) 257–265, <http://dx.doi.org/10.1007/BF02319666>.
- [4] J.S. Hawong, C.H. Lin, S.T. Lin, J. Rhee, R.E. Rowlands, A hybrid method to determine individual stresses in orthotropic composites using only measured

- isochromatic data, *J. Compos. Mater.* 29 (1995) 2366–2387.
- [5] J. Rhee, R.E. Rowlands, Thermoelastic-numerical hybrid analysis of holes and cracks in composites, *Exp. Mech.* 39 (1999) 349–355, <http://dx.doi.org/10.1007/BF02329816>.
 - [6] T.H. Baek, R.E. Rowlands, Experimental determination of stress concentrations in orthotropic composites, *J. Strain Anal. Eng. Des.* 34 (1999) 69–81.
 - [7] T. Baek, R. Rowlands, Hybrid stress analysis of perforated composites using strain gages, *Exp. Mech.* 41 (2001) 195–203.
 - [8] S.H. Ju, R.E. Rowlands, Mixed-mode thermoelastic fracture analysis of orthotropic composites, *Int. J. Fract.* 120 (2003) 601–621, <http://dx.doi.org/10.1023/A:1025557715318>.
 - [9] S.H. Ju, R.E. Rowlands, Thermoelastic determination of KI and KII in an orthotropic graphite-epoxy composite, *J. Compos. Mater.* 37 (2003) 2011–2025.
 - [10] A. Alshaya, X. Shuai, R. Rowlands, Thermoelastic stress analysis of a finite orthotropic composite containing an elliptical hole, *Exp. Mech.* 56 (2016) 1373–1384, <http://dx.doi.org/10.1007/s11340-016-0174-x>.
 - [11] M. Ashrafi, M.E. Tuttle, High strain gradient measurements in notched laminated composite panels by digital image correlation, in: G. Tandon (Ed.), *Compos. Hybrid Multifunct. Mater. Vol. 4 Proc. 2014 Annu. Conf. Exp. Appl. Mech.* Springer International Publishing, Cham, 2015, pp. 75–81, http://dx.doi.org/10.1007/978-3-319-06992-0_10.
 - [12] N.S. Fatima, Hybrid Photomechanical Full-field Stress Analysis of Orthotropic Composite Structures Containing Various Cutouts, PhD Thesis, University of Wisconsin-Madison, 2017.
 - [13] S.G. Lekhnitskii, *Anisotropic Plates*, Gordon & Breach Scientific Publishers, New York, 1968.
 - [14] I.M. Daniel, O. Ishai, *Engineering Mechanics of Composite Materials*, 2 edition, Oxford University Press, New York, 2005.
 - [15] F. Bisshopp, Numerical conformal mapping and analytic continuation, *Q. Appl. Math.* 41 (1983) 125–142.
 - [16] N.V. Challis, D.M. Burley, A numerical method for conformal mapping, *IMA J. Numer. Anal.* 2 (1982) 169–181.
 - [17] S.G. Lekhnitskii, *Theory of Elasticity of an Anisotropic Elastic Body*, first ed., Holden-Day, San Francisco, 1963.
 - [18] S.T. Lin, R.E. Rowlands, Hybrid stress analysis, *Opt. Lasers Eng.* 32 (1999) 257–298, [http://dx.doi.org/10.1016/S0143-8166\(99\)00057-3](http://dx.doi.org/10.1016/S0143-8166(99)00057-3).
 - [19] N. Muskhelishvili, *Some Basic Problems of the Mathematical Theory of Elasticity*, 1977 edition, Springer, Leyden, 1977.
 - [20] G.N. Savin, *Stress Concentration Around Holes*, Pergamon Press, 1961.
 - [21] A.A. Alshaya, Experimental, Analytical and Numerical Analyses of Orthotropic Materials and Biomechanics Application, PhD Thesis, University of Wisconsin-Madison, 2017.
 - [22] O.L. Bowie, C.E. Freese, Central crack in plane orthotropic rectangular sheet, *Int. J. Fract. Mech.* 8 (1972) 49–57, <http://dx.doi.org/10.1007/BF00185197>.
 - [23] T.D. Gerhardt, A hybrid/finite element approach for stress analysis of notched anisotropic materials, *J. Appl. Mech.* 51 (1984) 804–810, <http://dx.doi.org/10.1115/1.3167728>.
 - [24] Y.-M. Huang, Determination of Individual Stresses from Thermoelastically Measured Trace of Stress Tensor, PhD Thesis, University of Wisconsin-Madison, (n.d.).
 - [25] Correlated Solutions, Principle of Digital Image Correlation, (n.d). <http://www.correlatedsolutions.com/index.php/principle-of-digital-image-correlation>.
 - [26] N.S. Joglekar, Separating Stresses Using Airy's Stress Function and TSA, Effects of Varying the Amount and Source Locations of the Input Measured TSA Data and the Number of Airy Coefficients to Use, Master Thesis, University of Wisconsin-Madison, 2009.
 - [27] R. Venkatesh, S. Paneerselvam, R. Rowlands, Complete stress analysis of a mechanical joint from recorded data of single displacement component, *Exp. Appl. Mech.* 6 (2015) 23–41.
 - [28] M.H.A. Hamdi Abdelmohsen, Hybrid Experimental-Numerical Stress Analysis, PhD Thesis, University of Wisconsin-Madison, 1986.